GEOPHYSICS, VOL. 80, NO. 6 (NOVEMBER-DECEMBER 2015); P. D553–D563, 9 FIGS., 1 TABLE.
10.1190/GEO2015-0020.1

Full-wavefield modeling and reverse time migration of laser ultrasound data: A feasibility study

Jeffrey Shragge[1], Thomas E. Blum[2], Kasper van Wijk[3], and Ludmila Adam[4]

ABSTRACT

Laser ultrasound (LU) data acquired on cylindrical core samples effectively probe the physical properties of geologic materials. Although most LU analyses focus on estimating and inverting traveltimes of direct arrivals, it is important to recognize that LU data sets can have rich wavefield coda and can now be acquired with a sufficient spatial density to enable the application of exploration seismic full-wavefield techniques such as reverse time migration (RTM) and, potentially, full-waveform inversion (FWI). We have developed a feasibility study that examines the applicability of 2D acoustic forward modeling and 2D RTM analyses on laboratory LU data acquired on cylindrical polymer samples. Forward-modeled waveforms from our numerical tests matched the kinematics of the LU body waves measured through homogeneous samples, as well as the scattered wavefield generated by fractures induced in an otherwise-homogeneous medium. The scattered wavefield is then used in an RTM scheme to directly image millimeter-scale fracture structure.

INTRODUCTION

One of the most widely used approaches for studying the fine-scale structure of geologic materials is by examining cylindrical drill-core samples recovered from reservoir boreholes. Undertaking a suite of laboratory experiments on these samples commonly provides insights into the bulk mineral constituents and physical properties of a formation (e.g., P- and S-wave velocities, density, and wave velocity anisotropy), as well as revealing key indicators of fluid-flow potential such as porosity and permeability (Han et al., 1986; Vanorio et al., 2002; Guéguen et al., 2009). Similarly, time-lapse investigations on core samples can assist researchers in developing dynamic rock physics models of how geologic materials deviate from an initial insitu state (e.g., by changing confining pressure) (Prasad and Manghnani, 1997), how they react to fluid substitution (e.g., substituting brine, oil, and gases such as CO_2) (Winkler, 1985; Adam and Otheim, 2013), and how they react to geochemical rock alteration (e.g., rock-CO_2 reactivity) (Tompkins and Christensen, 2001).

The use of ultrasound for interrogating core samples to constrain rock physical estimates has a long history. Most elastic-wave experiments on rocks in the laboratory have used piezoelectric transducers (PT) as sources and receivers at megahertz frequencies (Birch, 1960; Pyrak-Nolte et al., 1990; Groenenboom and Falk, 2000). Although direct wavefield arrivals from such experiments have been very useful for estimating bulk P- and S-wave velocities and azimuthal variations thereof due to layering or anisotropy (Hornby, 1998; Wang, 2002; Sondergeld and Rai, 2011; Nardi et al., 2012), these data sets are inherently limited in their ability to image the finer millimeter-scale structure of core samples because of incomplete spatial sampling of the complex scattered wavefields measured by a limited number of often noisy (i.e., ringing) transducers that are noisy. We note that these issues can be partially addressed by increasing the number of PTs used in any experiment, as demonstrated in Sarout et al. (2014), which uses measured waveforms to examine the effects of saturation, heterogeneity, and anisotropy.

The development of high-fidelity laser interferometric (LI) receivers (Scruby and Drain, 1990) affords the possibility of examining not just wavefield first arrivals but also the scattered wavefield coda in laser-ultrasound (LU) experiments on geologic core samples (Scales and Malcolm, 2003; Blum et al., 2010, 2011a, 2011b, 2013, 2014; Lebedev et al., 2011). Moreover, the increasing auto-

Manuscript received by the Editor 12 January 2015; revised manuscript received 18 May 2015; published online 25 September 2015.
[1]The University of Western Australia, School of Earth and Environment and School of Physics, Centre for Energy Geoscience, Crawley, Australia. E-mail: jshragge@gmail.com.
[2]ETH Zurich, Institute of Geophysics, Zurich, Switzerland. E-mail: thomas.blum@erdw.ethz.ch.
[3]The University of Auckland, The Dodd-Walls Centre for Photonic and Quantum Technologies and the Department of Physics, Auckland, New Zealand. E-mail: k.vanwijk@auckland.ac.nz.
[4]The University of Auckland, School of Environment, Auckland, New Zealand. E-mail: l.adam@auckland.ac.nz.

mation of LU experimental setups allows for rapid acquisition of wavefield data at many locations on a core sample, which leads to the LU equivalents of 2D and 3D exploration seismic shot gathers. (Other authors have similarly reported this for different physical modeling applications [Pouet and Rasolofosaon, 1990; Bretaudeau et al., 2011].) Additional challenges exist when conducting LU analyses at realistic stress conditions, which is something fairly straightforward to achieve with PT observations; however, improvements in LU hardware (e.g., pressure vessels with optically transparent observation windows) and acquisition practice indicate that this represents a tractable undertaking (Adam et al., 2014).

These observations, along with the richness of measured LU wavefield coda, suggest that high-end exploration seismic imaging and inversion algorithms such as reverse time migration (RTM) (Baysal et al., 1983; McMechan, 1983; Whitmore, 1983) and full-waveform inversion (FWI) (Tarantola, 1984) are likely applicable in these contexts. (An example of the former may be found in Anderson et al. [2011], which applies RTM to LU data for nondestructive testing purposes.) If this assertion were proved correct, it would offer the tantalizing prospect of undertaking 3D full-wavefield modeling, RTM, and FWI experiments to generate high-resolution images and estimates of the elastic properties on physical scale lengths of a few millimeters to even a few hundred microns. Ideally, these images could contain the fine-scale geometric structure, and the physical and reservoir properties of core samples, not just representative bulk velocity values, and could be useful for constraining dynamic rock physics models for time-lapse monitoring applications (Adam et al., 2013).

We note that these 3D/4D imaging and inversion analyses would also be complementary to other geologic core investigation tools such as micro-CT scans that reveal the density and geometric properties, as well as optical microscopy that provide valuable information on rock mineralogy and pore-space distribution. For example, Prasad (2003) and Alam et al. (2011) demonstrate that elastic waves can be used to probe fluid flow units and to explore the correlation between elastic velocities and rock transport properties (i.e., pores and their connectivity). Micro-CT scans provide us with the microstructure of a rock, but to what extent elastic waves are sensitive to the observed microstructures requires more than a petrophysical analysis alone. Adam et al. (2014) shows that physical heterogeneity in terms of organics in shale samples does not always correspond with elastic heterogeneity. The method proposed herein could help unravel the rock microstructure as sensed by elastic waves. Integrating full-wavefield elastic imaging of pores and fractures with other physical data, such as estimates of microstructure from density contrasts in a CT scan, could aid in the development and testing of the finer details of rock physics models.

Table 1. Physical properties of PMMA materials

Physical property	Value
P-wave velocity α	2.64 km/s
S-wave velocity β	1.32 km/s
Density ρ	1.19 g/cm^3
Lamé parameter λ	4.15 GPa
Lamé parameter μ	2.07 GPa

We present a feasibility study of applying acoustic seismic modeling and RTM technologies to image laser ultrasonic data sets acquired on homogeneous and fractured polymer materials. We choose these materials because they represent ideal media for numerical testing of the "imaging system" (i.e., modeling a distributed source wavefield, subsequent wave propagation, and detection at a receiver), which represents a key initial step in demonstrating the feasibility of applying full-wavefield methods to LU data. Herein, we examine four questions that represent important steps toward addressing the above assertions: (1) How similar are measured LU waveforms to recorded exploration seismic data? (2) Can we accurately model LU wavefield propagation through cylindrical core samples? (3) Can we tailor industry-standard RTM algorithms to suit LU wavefields? (4) Can we image millimeter-scale structure (or even finer) using LU data sets? We will address these questions through a combination of physical laboratory experiments and numerical modeling and imaging tests.

We begin by discussing physical experiments through cylindrical polymethyl methacrylate (PMMA) samples using a PT source and an LI measurement apparatus (Blum et al., 2010). We show that the 2D LU data sets acquired in homogeneous and fractured PMMA samples exhibit identifiable body-wave arrivals as well as observable scattered waves appropriate for RTM imaging experiments. Subsequently, we discuss our approach for performing full-wavefield acoustic modeling through cylindrical objects and provide modeling results that aim to match LU observations. We then incorporate our wavefield modeling approach into an RTM algorithm and demonstrate its utility for producing images of fractured media at the millimeter scale using the scattered wavefield components. We conclude with a discussion on the applicability of the modeling and imaging approach to 3D complex media such as geologic drill-core samples, and we present our prospectus for an extension to FWI analyses.

LABORATORY EXPERIMENTS

This section describes two suites of LU experiments carried out on cylindrical PMMA samples. Detailed descriptions of the experimental setup and the data acquisition methodology may be found in Blum (2012). However, for completeness, we will provide a review of the experimental details that are germane to the present work below.

PMMA is a material commonly used in optical engineering experimentation, largely because it is an isotropic and low-loss medium (between 0.1 and 1.0 MHz frequencies [Capodagli and Lakes, 2008]) with well-known physical properties (see Table 1). This combination of factors makes it an excellent material for undertaking LU experiments under controlled laboratory settings. Figure 1 presents a photograph of one such PMMA sample formed as a cylinder with a diameter of 50.8 mm and a height of 150.0 mm, which are physical dimensions representative of those encountered in laboratory drill-core experiments.

Blum (2012) describes LU experiments involving a variety of PMMA samples and a combination of PT sources and an LI data acquisition system. Figure 2 illustrates the experimental geometry of the data acquisition for the data sets used herein. A 7.5-mm-diameter PT source is glued onto the PMMA cylinder and covers roughly a 12° surficial arc. A PT source is used to generate wavefield energy and is driven by a short and highly energetic 400 V pulse at its natural frequency, which is coupled elastically to the PMMA sample. The excited source wavefield propagates throughout the PMMA material and emerges at the free surface at later times where it induces small (vector) displacements whose radial component is recorded by the LI unit. Triggered at the onset of the PT energy pulse, the LI unit measures the vibrations as a time-series data set sampled at a very high rate (i.e., $\Delta t = 0.01$ μs). The LI is designed with an adaptive crystal that compensates for slow variations in the wavefront, effectively acting as an optical high-pass filter. This ensures that the signal produced by the LI corresponds only to high-frequency displacement created by the ultrasonic elastic waves. The frequency content of recorded waveforms largely fall between 0.25 and 1.20 MHz with amplitudes ranging between ± 0.4 nm. For reference, the wavelengths of 0.25 and 1.2 MHz P-waves in a homogeneous PMMA medium are 10.4 and 2.6 mm, respectively.

Using a single PT source and one LI detector generates an LU equivalent of a seismic trace (i.e., a time series for a single source-receiver pair). As illustrated in Figure 2, the locations of the source-receiver pair fix the *relative* experimental geometry by defining a central angle θ (taken in a clockwise fashion) between the origin, source, and receiver locations. We specify an *absolute* global coordinate system by ascribing the PT source location as Ψ degrees clockwise from the y-axis. Keeping the PT location constant, one may then repeatedly reposition the LI detector on the cylindrical surface and record additional traces with different acquisition geometries. We note that the combination of highly repeatable PT source waveforms and acquiring measurements over a full range of θ leads to the equivalent of a seismic shot gather. Finally, repeating the full experiments over a range of Ψ positions by moving the PT source location acquires the equivalent of a seismic survey that would be useful for high-resolution seismic imaging and inversion experiments.

Homogeneous polymethyl methacrylate sample

Figure 3a presents the LU shot-gather data set acquired through the homogeneous PMMA sample described above (i.e., equivalent to an undisturbed section of Figure 1). The data are plotted with a horizontal axis that is defined such that $\theta = 180^\circ$ represents a directly opposed source-receiver pair in a transmission geometry. Due to an inability to have the PT-LI system hardware too close together (i.e., interference), it was not possible to obtain a complete 360° angular swath and the shot gather is missing traces between roughly $-18^\circ < \theta < 18^\circ$. We observe a variety of different body-wave arrivals in the data set including the direct P-wave hyperbola (20 μs at $\theta = 180^\circ$), a direct S-wave hyperbola (39 μs at $\theta = 180^\circ$), a first-order P-P free-surface multiple (37 μs at $\theta = 320^\circ$), and a second-order P-P-P multiple (58 μs at $\theta = 180^\circ$). Closer examination of the direct-arrival waveforms reveals that the source-time function deviates from an idealized spatial delta function. Numerical tests demonstrated that the observed "doublet" is generated by a spatially distributed PT source spanning 12° of circumferential arc on the PMMA sample. This observation suggests that accurately simulating LU source wavefields for imaging and inversion purposes will require faithfully reproducing the spatial distribution of glued-on PT sources or whichever energy source is being employed (e.g., a laser).

Rayleigh waves are also present in the data set shown in Figure 3a. In this shot-profile geometry, Rayleigh waves circumnavigate the cylindrical sample and appear as events with linear moveout. Because these waveforms do not traverse the core interior and are thus insensitive to interior model parameters, they represent noise for the purposes of body-wave imaging and inversion experiments. We also observe what appears to be random noise prior to the first arrivals and at later times throughout the section. Figure 3b shows the data from Figure 3a after applying a dip filter, which

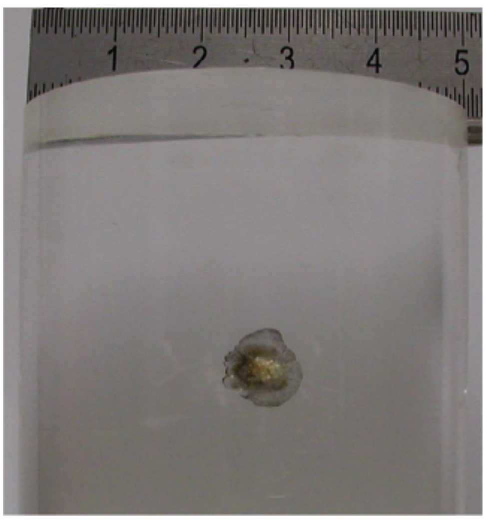

Figure 1. Photograph of the PMMA cylinder used for the LU testing after introducing a 7.5-mm crack offset from the center axis by roughly 1.5 mm.

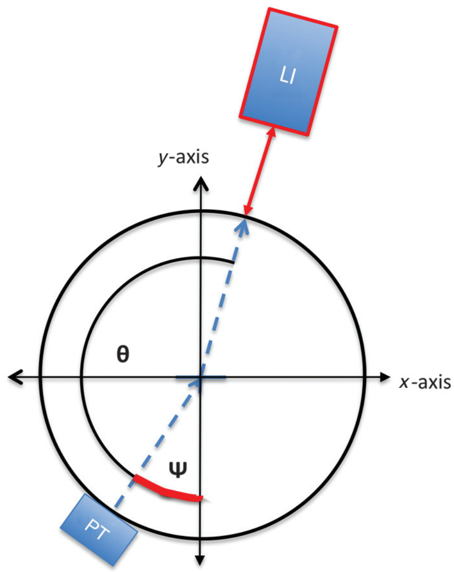

Figure 2. Schematic of the experimental setup used for LU data acquisition through PMMA cylinders. Central angle θ represents the angle formed the origin and the PT-LI detector pair "rays" indicated by the dashed blue lines, which ranges between $-180^\circ < \theta < -180^\circ$. Angle Ψ represents the angular deviation of the PT source from the reference y-axis, as illustrated by the thick red line. For the second suite of experiments on fractured PMMA material, we orient the y-axis normal to the fracture plane, which is shown by the thicker black line on the x-axis to either side of the origin.

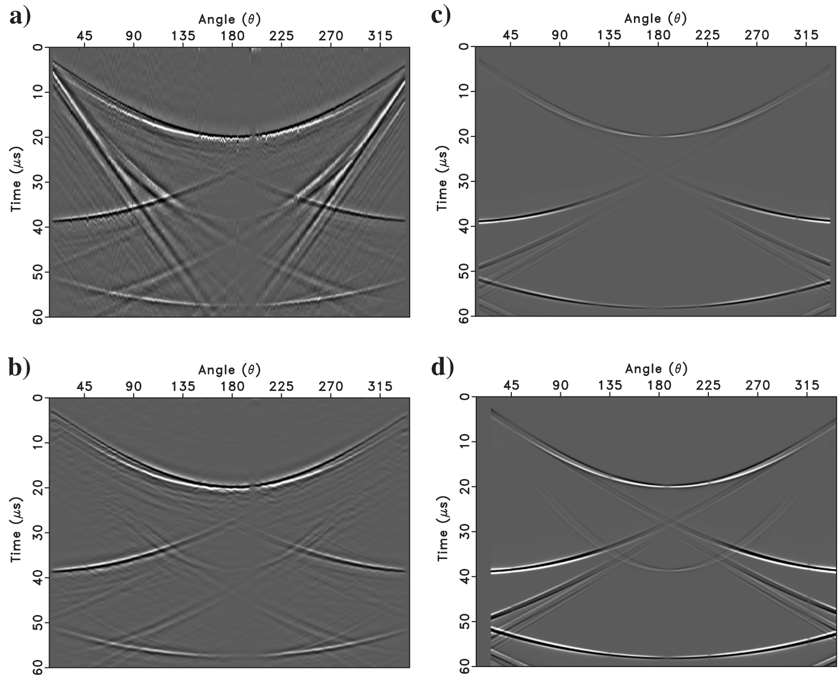

Figure 3. The LU data set acquired through a homogeneous PMMA cylinder using a PT source and a LI detector. (a) Measured shot-gather wavefield. (b) Data in (a) after applying a dip filter to remove the linear Rayleigh wave arrivals. (c) P-wave acoustic wavefield simulated through a 2D circular mesh in a P-wave velocity model based on PMMA material. (d) Acoustically modeled P- and S-wave data sets superimposed to form a single shot-gather data set.

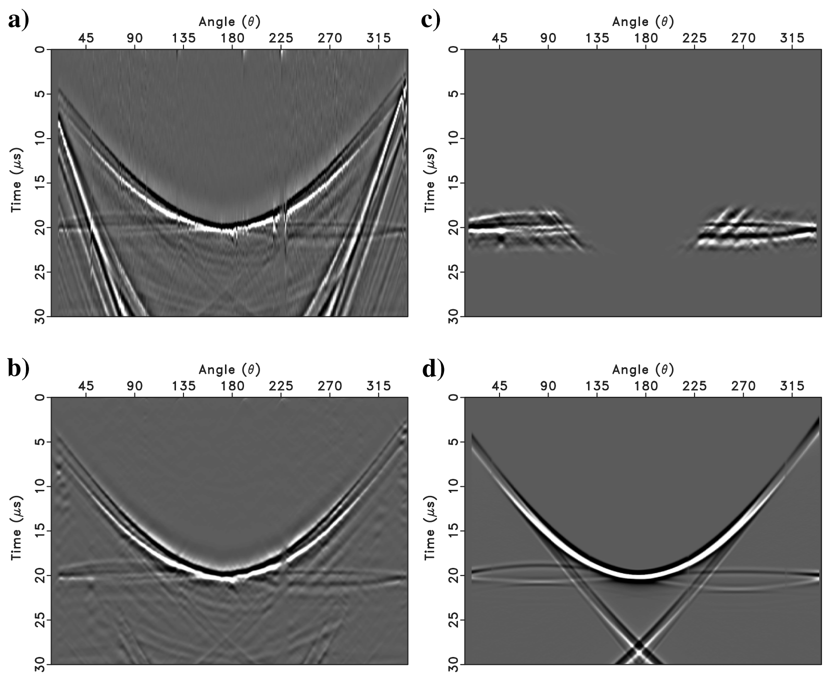

Figure 4. The LU data for a PT source located $\Psi = 0^{\circ}$ from the normal of the induced fracture. (a) LU data set acquired through the fractured PMMA sample shown in Figure 1. (b) Data in panel (a) after applying a dip filter to remove the linear Rayleigh wave arrivals. (c) Filtered and masked P-wave wavefield energy scattered off of the induced fracture. (d) Wavefield data extracted from the 2D acoustic wavefield simulated through a circular mesh using a velocity model incorporating a thin 7.5-mm-long crack offset by 1.5 mm from the axis of symmetry.

removes the linear Rayleigh arrivals but leaves the body waves largely untouched.

Fractured PMMA sample

We examine a second PMMA sample containing a single fracture in an otherwise homogeneous medium that was generated by collimating laser energy within the PMMA sample and thereby induced thermomechanical failure. Care was taken to ensure that the sample was remounted in the center of the stage, and computer control of stage motion ensured a repeatable receiver location to within a millimeter. Figure 1 shows the vertically oriented induced fracture as approximately 7.5 mm in diameter, less than 1 mm in thickness, and offset by approximately 1.5 mm from the vertical axis of symmetry. Shot-gather LU data sets similar to those shown in Figure 3a–3b were acquired through the center of the fracture for two different PT source locations at angles of $\Psi = 0^{\circ}$ and 50°.

Figure 4a shows the LU data acquired for a source oriented at $\Psi = 0^{\circ}$ to the normal of the fracture plane. (The second data set acquired at $\Psi = 50^{\circ}$ is presented in Blum et al. (2011a) and is omitted for brevity herein.) As expected, there is a strong similarity between this data set and that shown in Figure 3a. Figure 4b similarly presents dip-filtered waveforms comparable to those shown in Figure 3b. We note that the induced fracture has generated additional scattered wavefield components that arrive in the range of 17–22 μs at all θ angles. To better illustrate the scattered wavefield components, Figure 4c shows filtered and masked scattered wavefield arrivals. These arrivals are split into at least two distinct waveforms, with the different "limbs" generated by diffractions from the fracture tips. The temporal separation between the two diffraction limbs is dependent on the fracture length, whereas the asymmetry in the arrivals between θ blocks to either side of $\theta = 180^{\circ}$ is due to the 1.5-mm shift off of the symmetry axis.

The LU data sets acquired in the physical experiments give rise to a few interesting observations and questions that directly impact the acoustic modeling and imaging experiments described below. The first question is, How accurately can one model the kinematics (let alone the dynamics) of the PT source wavefield? Successfully addressing this issue requires modeling, at minimum, a distributed acoustic source to generate the observed doublet waveform. A second question is how well can one recover the various body-wave arrivals noted in the waveforms for a homogeneous cylinder? This will require accurately simulating wavefield propagation within the cylindrical geometry and enforcing the reflecting boundary conditions at the edges of the model domain. Finally, how accurately can one model the scattered wavefield components from millimeter-scale heterogeneity such as those caused by the fractured PMMA sample? This will require introducing, and thereby demonstrating a sensitivity to, additional model complexity. We address these questions in the following section.

ACOUSTIC FORWARD MODELING

Numerically simulating 2D and 3D acoustic wavefields through cylindrical models offers a different set of numerical challenges from computing wavefield propagation through Cartesian exploration-scale earth models. Three key differences to be addressed are (1) how to specify a computational mesh that matches the cylindrical geometry, (2) how to accurately describe the physics of acoustic wave propagation on the developed cylindrical mesh, and (3) how to choose a numerical approach that accurately solves the corresponding acoustic wave equation.

There are a variety of different numerical wavefield simulation techniques that can be used to address these wavefield modeling challenges on non-Cartesian meshes, including finite-difference (Shragge, 2014b), finite-element (Marfurt, 1984), spectral-element (Komatitsch and Vilotte, 1998), and discontinuous-Galerkin (Cockburn et al., 2000) approaches. Likewise, one could choose different physics (e.g., acoustic or elastic), whether or not to include attenuation, as well as the solution domain (time or frequency). For the numerical experiments described herein, we elect to use a 2D/3D nonattenuating acoustic finite-difference time-domain (FDTD) modeling tool described in Shragge (2014b). However, we recognize that other modeling approaches may be more computationally efficient and/or more physically or numerically accurate than the approach described, and we emphasize that the chosen seismic modeling approach should be tailored to match the characteristics of the problem at hand.

A detailed exposition of the wavefield modeling technique followed herein is beyond the scope of the current discussion; however, we provide a brief summary for completeness and refer readers to Shragge (2014b) for details of the 2D/3D acoustic FDTD approach. By definition, the physics of acoustic wave propagation is governed by a coordinate-independent acoustic wave equation. Most applications involving computing numerical solutions to the 3D acoustic wave equation are based on a Cartesian coordinate system herein defined by symbol $\mathbf{x}$. Consequently, most practitioners are familiar with the Cartesian acoustic wave equation and corresponding FDTD solution approaches.

However, in some wavefield modeling problems involving non-Cartesian geometry, it is advantageous to solve the 3D acoustic wave equation in a more generalized coordinate system $\boldsymbol{\xi}$ that better conforms to the topology of the problem being addressed (e.g., a cylinder). Modeling acoustic pressure wavefields throughout a generalized domain $\boldsymbol{\xi} \in \Omega$ requires solving a more generalized acoustic wave equation:

$$\left[\nabla^2_{\boldsymbol{\xi}} - \frac{1}{v^2_{\boldsymbol{\xi}}}\frac{\partial^2}{\partial t^2}\right]\mathcal{S}(\boldsymbol{\xi}, t) = 0 \quad \text{for } t \geq 0, \tag{1}$$

subject to pressure wavefield state on the domain boundary $\partial\Omega$

$$\mathcal{S}(\partial\Omega, t) = \mathcal{S}_0(\partial\Omega, t) \quad \text{for } t \geq 0, \tag{2}$$

where $\nabla^2_{\boldsymbol{\xi}}$ is the Laplacian operator in the specific generalized $\boldsymbol{\xi}$-coordinate system, $v_{\boldsymbol{\xi}}$ is the velocity model in the $\boldsymbol{\xi}$-coordinate system, $\mathcal{S}$ is the desired source wavefield solution, and $\mathcal{S}_0$ is the distributed source function. Note that the values of $\mathcal{S}$ must be weighted correctly to account for the non-Cartesian geometry and that the simulated wavefield solution $\mathcal{S}(\boldsymbol{\xi}, t)$ should be interpolated back to Cartesian coordinates $\mathcal{S}(\mathbf{x}, t)$ for visualization purposes.

Specifying the Laplacian operator $\nabla^2_{\boldsymbol{\xi}}$ in non-Cartesian geometry requires introducing additional geometric fields into the acoustic wave equation that account for spatial variability of the coordinate geometry. By incorporating concepts from differential geometry, Shragge (2014b) obtains a generalized 3D acoustic wave equation, demonstrates how to implement a standard $O(\Delta x^8, \Delta t^2)$ FDTD approximation scheme to compute $\mathcal{S}(\boldsymbol{\xi}, t)$ wavefield solutions, and shows how to interpolate these solutions back to the physical Cartesian domain $\mathcal{S}(\mathbf{x}, t)$ wavefields.

Because we examine acoustic wave propagation through cylindrical objects, we assert that using 2D circular meshes (or cylindrical grids in 3D) is more natural than Cartesian meshes because the $\partial\Omega$ computational domain boundary can be tailored to match the topology of the cylindrical model surface. Doing so allows us to more easily implement the reflecting free-surface boundary condition and to more accurately simulate the internal reflections from this boundary observed in the data sets above. Shragge (2014b) provides the theory and numerical examples of wave propagation in a semiorthogonal 3D cylindrical mesh formed by an (invertible) analytic mapping between a cylinder and a cube. However, because the LU data described in the experiments below were acquired in 2D slices, we restrict our examples to a 2D circular disk shown in Figure 5.

Homogeneous polymethyl methacrylate sample

We create a 2D computational mesh of size 512×512 by rescaling the meshed disk of unit radius shown in the top plane in Figure 5 to match the physical dimensions of a cross section of the cylindrical PMMA sample shown in Figure 1. We assume a homogeneous

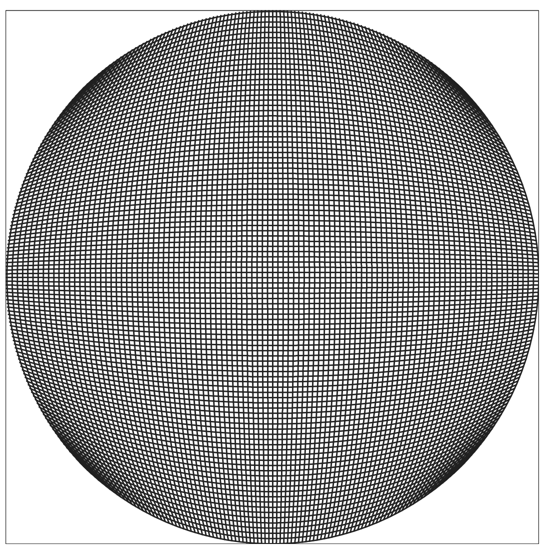

Figure 5. The 2D computational mesh used to simulate 2D acoustic wavefields using the generalized FDTD approach.

velocity model v_ξ equal to that of the PMMA velocity given in Table 1. To create the doublet source wavefield noted in the above data sets, we use a 2D distributed source wavefield formed by a 2D Gaussian wavelet with a 0.4-MHz central frequency spread over a 12° circumferential arc.

We simulate 90 μs of 2D acoustic wavefield propagation at a temporal sampling rate of $\Delta t = 0.03$ μs by iteratively following a three-step procedure: (1) injecting the 2D distributed source function into a propagating wavefield on the domain boundary, (2) forward modeling the propagating wavefield by a single Δt time step, and (3) extracting the boundary wavefield values to form the simulated data set. We repeat this procedure for all 3000 time steps until we have fully computed the synthetic data set. For visualization purposes, we interpolate the data sections below from the generalized $\boldsymbol{\xi}$-domain to a Cartesian $\mathbf{x}$-domain using 2D sinc operators.

Figure 6 presents nine wavefield snapshots of the propagating acoustic wavefield starting at $t = 12.0$ μs and then taken every $\Delta t = 7.5$ μs to a maximum time of $t = 72.0$ μs. Figure 6a shows the earliest wavefield snapshot that most readily demonstrates that the 2D distributed Gaussian source function generates a doublet

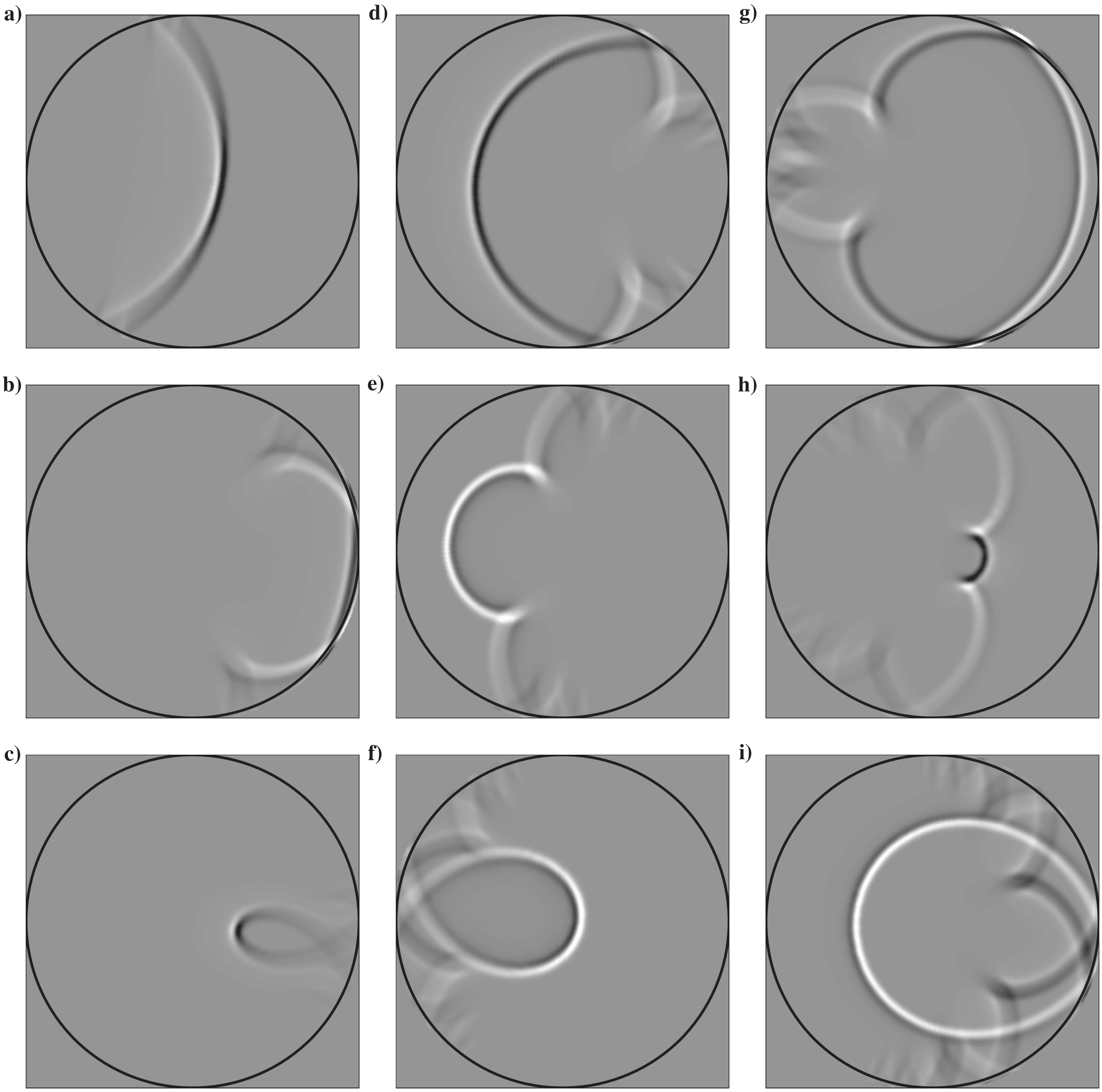

Figure 6. The 2D wavefield snapshots of source wavefield $\mathcal{S}(\mathbf{x}, t)$ propagating in disk with perfectly reflecting boundaries for a modeled 0.4 MHz PT source function distributed across 12° of circumferential arc: (a) $t = 12.0$, (b) 19.5, (c) 27.0, (d) 34.5, (e) 42.0, (f) 49.5, (g) 57.0, (h) 64.5, and (i) 72.0 μs.

wavefield similar to that shown in Figure 3a. Because some wavefield components continuously propagate in proximity to the curved free surface, they will continuously produce free-surface-reflected wavefield components that subsequently propagate back into the interior. Figure 6b shows the wavefield as the direct arrivals are reaching the far side at $\theta = 180^{\circ}$. The reflected wavefield then collapses into a “bow-tie” (Figure 6c) because it propagates back toward the source location (Figure 6d). Note that a chain of multiply reflected events has formed behind the main singularly reflected wavefield component. The subsequent panels show wavefield snapshots up to an additional two-way transit through the sample, which generates an even more complex train of multiply reflected wavefield events.

Figure 3c shows the shot-gather data set extracted from the boundary of the propagating wavefield in Figure 6 after interpolation back to a Cartesian mesh. The modeled data show good kinematic agreement with many of the P-wave waveforms noted in Figure 3b, including the direct arrivals and the singly and doubly reflected contributions. In addition, several higher order multiple reflections are visible at times greater than 40 μs. The amplitudes of wavefield arrivals show broad agreement with the recorded data; however, additional work is required to improve the amplitude accuracy through a better representation of the injected distributed source function and a better accountance for elastic wavefield behavior (i.e., S- and Rayleigh waves).

We subsequently repeat the above acoustic propagation experiment using a similar 2D distributed source function, but with a model of the S-wave velocity of the PMMA material. Figure 3d shows the superimposition of the S-wave data set with the previously discussed P-wave data set (in which the S-wave model is scaled by a 0.1× factor). This panel shows that we can model the observed S-wave arrivals (though no P-S or S-P mode conversions due to modeling assumptions), which are observed between 35 and 40 μs at $\theta = 180^{\circ}$. However, these waveforms exhibit lower kinematic and dynamic accuracy, and we will thus restrict discussion in the remainder of the paper to the compressional body wave.

Fractured polymethyl methacrylate sample

To simulate an acoustic wavefield through a fractured PMMA sample, we repeat the 2D forward-modeling procedure described above, save for introducing a P-wave velocity model containing a single fracture. Figure 7 shows a schematic of the model incorporating a 0.2-mm-thick and 7.5-mm-long fracture offset from the axis symmetry in the ξ_1 direction by 1.5 mm and having P-wave velocities of 2.6 and 2.0 km/s for the background and fracture components, respectively. We center the distributed 2D source function at $\Psi = 0^{\circ}$ to the y-axis normal to optimally match the waveforms shown in Figure 4b.

Figure 4d presents wavefield data simulated through the fractured velocity model shown in Figure 7. The kinematics of the P-wave direct arrivals again are quite consistent with those in the physical LU experiments. We also observe that the fracture model has generated additional wavefield scattering that closely resembles that with Figure 4a–4c. In particular, we observe the two different scattering limbs from the fracture tips where those between $0^{\circ} < \theta < 180^{\circ}$ arrive in advance of those between $180^{\circ} < \theta < 360^{\circ}$. This suggests that shifting the fracture off-axis by 1.5 mm in the numerical model is roughly in line with that measured in the physical PMMA sample. We also note that the maximum separation between the two limbs on either side of $\theta = 180^{\circ}$ is roughly 3 μs in the numerical and physical experiments, which suggests that the modeled 7.5-mm fracture length is fairly representative of the fractured PMMA sample. Overall, these numerical tests demonstrate an ability to accurately model the kinematics of 2D wavefield propagation including boundary reflections and scattering off of millimeter-scale structure within cylindrical drill cores.

REVERSE TIME MIGRATION OF FRACTURED POLYMETHYL METHACRYLATE LASER ULTRASOUND DATA

Conventional Cartesian acoustic RTM is based on computing numerical solutions of a forward-modeled source and an (ideally) singly scattered receiver wavefield $\mathcal{S}(\mathbf{x}, t)$ and $\mathcal{R}(\mathbf{x}, t)$. Singly scattered refers to a physical model in which the interaction of the source wavefield with discontinuous model structure generates a secondary or scattered wavefield that itself does not interact with other discontinuous structure as it propagates to, and is recorded at, receiver locations. The first algorithmic step of our RTM procedure is to forward model $\mathcal{S}$ from time $t = 0$ to $t = T_{\max}$ using the acoustic FDTD procedure described above. The modeled source wavefield is then reversed in time and stepped backward (i.e., anticausally) from $t = T_{\max}$ to $t = 0$ using the adjoint of the FDTD forward-modeling procedure described above. In lock step with the backward propagating source wavefield, a receiver wavefield is formed by injecting recorded data (i.e., a shot gather) into $\mathcal{R}(\mathbf{x}, t)$ and propagating one step backward in time. This two-step procedure is repeated from time $t = T_{\max}$ to $t = 0$. An RTM image $\mathcal{I}(\mathbf{x}, t)$ is formed at each time step by evaluating an imaging condition based on the temporal summation of either a point-by-point multiplication of the $\mathcal{S}$ and $\mathcal{R}$ wavefields (Claerbout, 1985) or a slightly more involved “inverse-scattering” imaging condition involving correlation of wavefields postapplication of spatial and weighted temporal derivatives filters to $\mathcal{S}$ and $\mathcal{R}$ (Whitmore and Crawley, 2012).

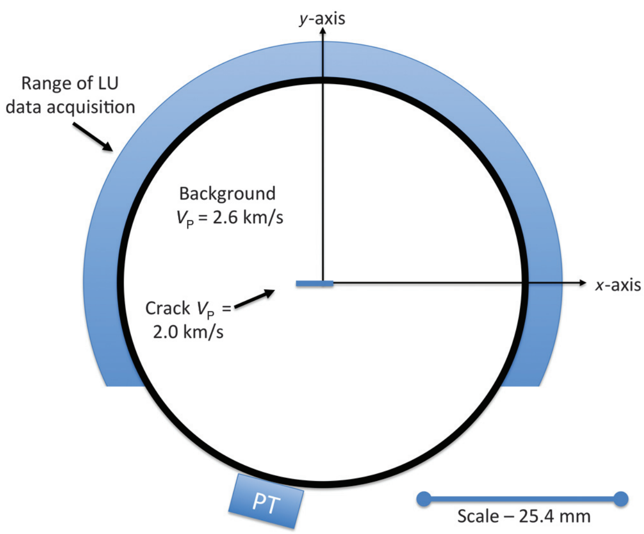

Figure 7. A schematic of the P-wave velocity model used to simulate the fractured PMMA medium from the physical experiments. The modeled fracture is 7.5 mm long, offset 1.5 mm along the x-axis from the origin and has P-wave velocities of 2.6 and 2.0 km/s for the background and fractured components, respectively.

Applying this Cartesian RTM procedure in a more generalized coordinate system represents a fairly straightforward extension (Shragge, 2014a). The three main differences are that (1) the simulated $\mathcal{S}(\boldsymbol{\xi}, t)$ and $\mathcal{R}(\boldsymbol{\xi}, t)$ wavefields must be solutions to the acoustic wave equation appropriate for the $\boldsymbol{\xi}$-coordinate system, (2) one must account for non-Cartesian geometry if using an inverse-scattering imaging condition, and (3) the final RTM image should be interpolated back to Cartesian coordinates for visualization purposes (i.e., $\mathcal{I}(\boldsymbol{\xi}, t) \rightarrow \mathcal{I}(\mathbf{x}, t)$).

Figure 8 presents six wavefield snapshots of receiver wavefield $\mathcal{R}(\mathbf{x}, t)$ as it propagates in reverse time from $t = T_{\max}$ to $t = 0$. This example is formed by injecting the filtered and masked data from Figure 4c into $\mathcal{R}(\boldsymbol{\xi}, t)$ during the time-reverse propagation. The vertical black line indicates the modeled fracture location (Figure 7). Figure 8a–8c shows $\mathcal{R}(\mathbf{x}, t)$ as it coalesces back to the points in time and space when and from which it scattered. Figure 8d shows $\mathcal{R}(\mathbf{x}, t)$ at the time when the source wavefield scattered off of the crack. Interestingly, the time-reversed wavefield energy is concentrated at the fracture tips and appears to image an observable radiation pattern. Figure 8e–8f shows $\mathcal{R}(\mathbf{x}, t)$ as it propagates back toward $t = 0$. We note that for this (relative) simple model, we can fairly accurately estimate the time when scattering happened; however, this is unlikely to be the situation in general for more complex materials such as a geologic drill core.

Figure 9 presents the RTM imaging results generated via an inverse-scattering imaging condition for the shot-gather data set discussed in the section "Fractured polymethyl methacrylate sample" above with a 5-mm grid overlain for reference. The proportions of the imaged PMMA fracture are roughly in line with the physical PMMA fracture shown in Figure 1: approximately 7.5 mm in length with a thickness of about 1–2 mm, falling along the x-axis but offset from the y-axis by roughly 1.5 mm. However, because we have used a 0.4-MHz central frequency source wavelet, the image is band limited and will suffer from $\lambda/4 = 1.6$-mm (Fresnel) resolution limits for PMMA media. Thus, the imaged fracture thickness is thicker than one should expect by visual inspection of the physical PMMA sample. Finally, whereas in 3D exploration seismology, it is common to image the subsurface with tens to hundreds of thousands of sources, herein, we have constructed this RTM image using only a single shot gather. Accordingly, we expect that imaging the fracture at a variety of different Ψ source angles would both help to improve the image signal-to-noise characteristics by stacking away single-shot artifacts and enhance image resolution closer to the theoretical $\lambda/4$ limit.

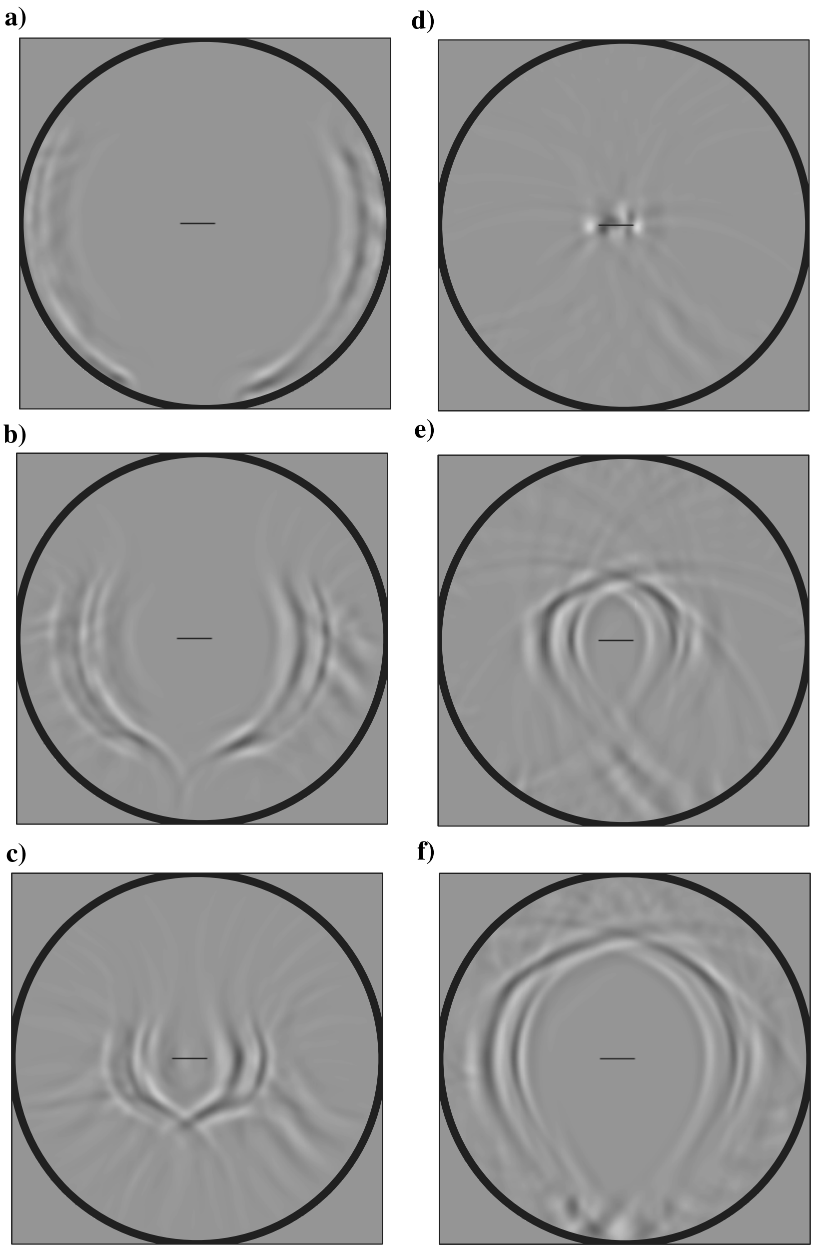

Figure 8. Back-propagating wavefield snapshots of the scattered $\mathcal{R}(\mathbf{x}, t)$ wavefield after interpolation to Cartesian: (a) $t = 19.8$, (b) 16.8, (c) 13.8, (d) 10.8, (e) 7.8, and (f) 4.8 μs.

DISCUSSION

The "Introduction" section posed four questions that we would like to address in this discussion. The first question is, How similar are measured LU waveforms to recorded exploration seismic data? The data sets presented above illustrate that LU waveforms can be acquired with sufficient fidelity and trace density to effectively represent exploration shot gathers. Although we discuss only a single shot-gather experiment using PT sources, we emphasize that recent developments in laser source technology and the near automation of LI data acquisition now enable practical recording of a large 2D and, more sparsely, 3D shot gathers within a reasonable time frame.

Second, can we accurately model LU wavefield propagation through cylindrical core samples? Herein, we use a 2D acoustic FDTD modeling approach that reproduces wavefield kinematics quite well; however, we recognize that the dynamics of our simulation are not yet at a point at which we can match amplitudes with a high degree of confidence. We assert that doing so would require a better understanding of a variety of experimental issues that affect amplitude: modeling of distributed sources waveforms, elastic propagation effects including anisotropy, inclusion of attenuation and/or scattering phenomena, poroelastic behavior, and accounting for the transfer function of the LI instrumentation. We note that a significant body of work exists in the fields of engineering and nondestructive testing around the use of ultrasonics and elastic wavefield scattering in fractured media (Pecorari, 2003; Broda et al., 2014) that could provide insight into the wavefield behavior in observed LU data sets. Future work will examine these important and unresolved questions in more detail, including experimentation using well-benchmarked spectral element modeling codes (Komatitsch and Vilotte, 1998) that have been shown to accurately model a wider range of viscoelastic wavefield behavior.

Third, can we tailor industry-standard RTM algorithms to suit LU wavefields? The numerical experiments described herein indicate that we may readily adapt industry-standard RTM algorithms to the problem of imaging LU data sets acquired on drill core. Although this does not pose an algorithmic challenge, we assert that performing effective 2D RTM imaging on more complex geologic materials will require significantly denser LU acquisition ideally involving scores of shot profiles for 2D applications. For 3D applications, this may require measuring hundreds of 3D shot profiles and we recognize that this would bring data acquisition and computational challenges. However, within our group of authors, we have been able to record 3D LU data sets and perform 3D acoustic wavefield simulations, and we are thus well positioned to argue that these do not represent intractable technical challenges.

Fourth, can we image millimeter-scale structure (or even finer) using LU data sets? The RTM results presented herein indicate that it is possible to image small-scale structures down to the millimeter scale, which, for 0.4-MHz P-waves in PMMA material, is close to the $\lambda/4 = 1.6$ mm (Fresnel) resolution criteria. One improvement could be to use pulsed lasers as sources of mechanical energy. Such lasers can generate very short and intense impulses of light that get absorbed by a sample surface, causing thermoelastic expansion, in turn generating an elastic wave. Laser-generated sources can be easily positioned due to their noncontacting property, and they also generate broadband wavefields, in particular those containing higher frequencies than used here. It is unclear, though, whether or not geologic core samples would attenuate these higher frequency components and lead to only modest gains in resolution. We also argue that an incremental improvement in resolution could be realized by incorporating additional sources distributed around the circumference of the core sample into the RTM analysis. In addition, we point out that recent exploration seismic FWI studies have demonstrated an ability to resolve structure to within $\lambda/8 - \lambda/10$ under "ideal" conditions. Achieving this for LU applications on a drill core would translate to resolution on scale lengths of a few hundreds of microns, an observation that clearly helps incentivize our research in this direction. Potential applications of combining RTM and LU for time-lapse imaging of core samples may include monitoring fluid saturation distribution (Lebedev et al., 2009), rock microstructural changes due to rock-fluid reactions (Vialle and Vanorio, 2011; Adam et al., 2013), and elastic wave sensitivity to fractures and stress (Todd and Simmons, 1972; Lockner, 1993).

Our final question is, What is our prognosis for 2D and 3D FWI applications? Given the clear motivation of applying FWI analyses to LU data sets acquired through the drill core, we feel that it is important to list what we see as the key advantages and challenges in making this technology "work" in these scenarios. One advantage of applying FWI to LU data is that, unlike in exploration seismic applications, we can locate sources and receivers freely over the entire surface of the core sample and measure the complete transmitted wavefields. In contrast with surface-based seismic exploration, transmitted wavefields are generally only available due to vertical velocity gradients that generate turning-wave components measurable at far offsets. Second, one could also incorporate density and geometry information from CT scans that would serve as excellent a priori constraints for FWI. Interestingly, CT scans acquired on the fractured PMMA sample discussed herein could not pick up the small-scale fracture; however, there are clearly wavefield scattering effects visible in the LU data (Blum et al., 2013). This strengthens the argument for the need for incorporating complementary analyses into a more complete picture of geologic core sample.

There are several key challenges that would have to be addressed, though, to make FWI viable. These include accounting for the scattering and intrinsic (poroelastic) attenuation losses of propagating waves, an increased likelihood of anisotropic behavior, and a strong dependence on accurately modeling the dynamics of PT or thermoelastic coupling and the LI detector transfer function. It is likely that each of these issues would have to be addressed before one could realize a successful FWI application on LU data. Just as in exploration seismic FWI applications, though, if one could fully address these issues, then we assert that the inversion results could lead to impressive and important insights into our understanding of geologic materials and lead to new theories that better explain 3D/4D rocks physics behavior.

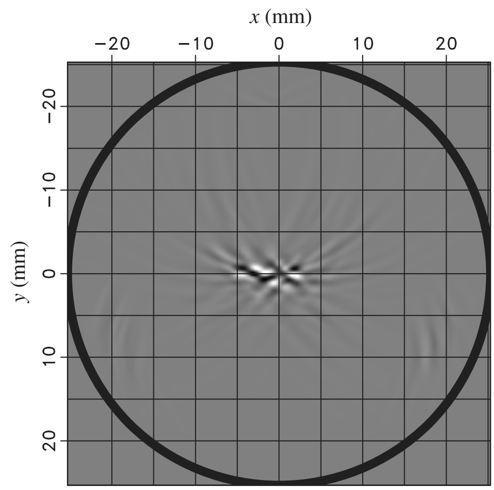

Figure 9. RTM fracture image for the scattered wavefield components shown in Figure 4c with a 5-mm grid to help constrain the proportions of the imaged fracture.

CONCLUSIONS

We present a feasibility study to show that full-wavefield modeling and RTM imaging analyses are applicable to 2D (and by extension to 3D) LU data acquired on geologic core samples using a laser interferometer acquisition system. We demonstrate that one may apply 2D generalized FDTD acoustic wave solvers on 2D circular (or cylindrical in 3D) meshes at wellbore drill-core scale and provide millimeter-scale grid resolution. We show that the kinematics of complex source effects may be reproduced through a judicious specification of distributed source-time functions and that acoustic wavefield simulation through cylindrical drill-core models can reproduce the kinematics of the direct arrivals and multiply scattered body-wave energy. We show that exploration-scale RTM can be adapted to the geometry and scale length of geologic core and that one may image structural heterogeneity within samples such as fractures on a millimeter-scale length (or smaller). Finally, these tests suggest that LU may be applicable for undertaking FWI studies; however, we caution that one must choose the correct physics and an accurate numerical strategy for modeling wave propagation and ensure that the acquisition geometry of LU data is sufficient to support full-wavefield inversion analyses.

ACKNOWLEDGMENTS

We thank Geophysics assistant editor V. Socco, associate editor M. Prasad, reviewers S. Mallick, B. Bonner, J. Sarout, and a fourth anonymous reviewer for comments that improved the original manuscript. J. Shragge acknowledges the support of the UWA Research Collaboration Grant, D. Lumley and colleagues at the Centre for Energy Geoscience, and sponsors of the UWA:RM consortium. L. Adam acknowledges the support of a University of Auckland travel grant. This work was supported by resources provided by the Pawsey Supercomputing Centre with funding from the Australian government and the government of Western Australia. Reproducible numerical examples were generated using the Madagascar package (http://www.ahay.org).

REFERENCES

Adam, L., and T. Otheim, 2013, Elastic laboratory measurements and modeling of saturated basalts: Journal of Geophysical Research: Solid Earth, **118**, 840–851, doi: 10.1002/jgrb.50090.

Adam, L., F. Ou, L. Strachan, J. Johnson, and K. van Wijk, 2014, Mudstone P-wave anisotropy measurements with non-contacting lasers under confining pressure: 84th Annual International Meeting, SEG, Expanded Abstracts, 1423–1440.

Adam, L., K. van Wijk, T. Otheim, and M. Batzle, 2013, Changes in elastic wave velocity and rock microstructure due to basalt-CO_2-water reactions: Journal of Geophysical Research: Solid Earth, **118**, 4039–4047, doi: 10.1002/jgrb.50302.

Alam, M. M., I. L. Fabricius, and M. Prasad, 2011, Permeability prediction in chalks: AAPG Bulletin, **95**, 1991–2014, doi: 10.1306/03011110172.

Anderson, B. E., M. Griffa, P.-Y. L. Bas, T. J. Ulrich, and P. A. Johnson, 2011, Experimental implementation of reverse time migration for nondestructive evaluation applications: Journal of the Acoustical Society of America, **129**, EL8–EL14, doi: 10.1121/1.3526379.

Baysal, E., D. Kosloff, and J. Sherwood, 1983, Reverse-time migration: Geophysics, **48**, 1514–1524, doi: 10.1190/1.1441434.

Birch, F., 1960, The velocity of compressional waves in rocks to 10 kilobars: 1.: Journal of Geophysical Research, **65**, 1083–1102, doi: 10.1029/JZ065i004p01083.

Blum, T., 2012, Characterization of heterogeneous media with multicomponent laser ultrasonics: Ph.D. thesis, Boise State University.

Blum, T., R. Snieder, K. van Wijk, and M. Willis, 2011a, Theory and laboratory experiments of elastic wave scattering by dry planar fractures: Journal of Geophysical Research, **116**, B08218, doi: 10.1029/2011JB008295.

Blum, T., K. van Wijk, R. Snieder, and M. Willis, 2011b, Laser excitation of a fracture source for elastic waves: Physical Review Letters, **107**, 275501, doi: 10.1103/PhysRevLett.107.275501.

Blum, T., K. van Wijk, B. Pouet, and A. Wartelle, 2010, Multicomponent wavefield characterization with a novel scanning laser interferometer: Review of Scientific Instrumentation, **81**, 073101, doi: 10.1063/1.3455213.

Blum, T. E., L. Adam, and K. van Wijk, 2013, Noncontacting benchtop measurements of the elastic properties of shales: Geophysics, **78**, no 3, C25–C31, doi: 10.1190/geo2012-0314.1.

Blum, T. E., K. van Wijk, and R. Snieder, 2014, Scattering amplitude of a single fracture under uniaxial stress: Geophysical Journal International, **197**, 875–881, doi: 10.1093/gji/ggu039.

Bretaudeau, F., D. Leparoux, O. Durand, and O. Abraham, 2011, Small-scale modeling of onshore seismic experiment: A tool to validate numerical modeling and seismic imaging methods: Geophysics, **76**, no. 5, T101–T112, doi: 10.1190/geo2010-0339.1.

Broda, D., W. J. Staszewski, A. Martowicz, and V. Silberschmidt, 2014, Modelling of nonlinear crack-wave interactions for damage detection based on ultrasound — A review: Journal of Sound and Vibration, **333**, 1097–1118, doi: 10.1016/j.jsv.2013.09.033.

Capodagli, J., and R. Lakes, 2008, Isothermal viscoelastic properties of PMMA and LDPE over 11 decades of frequency and time: A test of time-temperature superposition: Rheologica Acta, **47**, 777–786, doi: 10.1007/s00397-008-0287-y.

Claerbout, J., 1985, Imaging the earth's interior: Stanford University.

Cockburn, B., G. Karniadakis, and C. Shu, 2000, Discontinuous Galerkin methods: Theory, computation and applications: Springer-Verlag.

Groenenboom, J., and J. Falk, 2000, Scattering by hydraulic fractures: Finite-difference modeling and laboratory data: Geophysics, **65**, 612–622, doi: 10.1190/1.1444757.

Guéguen, Y., J. Sarout, J. Fortin, and A. Schubnel, 2009, Cracks in porous rocks: Tiny defects, strong effects: The Leading Edge, **28**, 40–47, doi: 10.1190/1.3064145.

Han, D.-H., A. Nur, and D. Morgan, 1986, Effects of porosity and clay content on wave velocities in sandstones: Geophysics, **51**, 2093–2107, doi: 10.1190/1.1442062.

Hornby, B. E., 1998, Experimental laboratory determination of the dynamic elastic properties of wet, drained shales: Journal of Geophysical Research: Solid Earth, **103**, 29945–29964, doi: 10.1029/97JB02380.

Komatitsch, D., and J.-P. Vilotte, 1998, The spectral element method: An efficient tool to simulate the response of 2D and 3D geological structures: Bulletin of the Seismological Society of America, **88**, 368–392.

Lebedev, M., A. Bona, R. Pevzner, and B. Gurevich, 2011, Elastic anisotropy estimation from laboratory measurements of velocity and polarization of quasi-P-waves using laser interferometry: Geophysics, **76**, no. 3, WA83–WA89, doi: 10.1190/1.3569110.

Lebedev, M., J. Toms-Stewart, B. Clennell, M. Pervukhina, V. Shulakova, L. Paterson, T. Müller, B. Gurevich, and F. Wenzlau, 2009, Direct laboratory observation of patchy saturation and its effects on ultrasonic velocities: The Leading Edge, **28**, 24–27, doi: 10.1190/1.3064142.

Lockner, D., 1993, The role of acoustic emission in the study of rock fracture: International Journal of Rock Mechanics and Mining Sciences & Geomechanics Abstracts: **30**, 883–899, doi: 10.1016/0148-9062(93)90041-B.

Marfurt, K., 1984, Accuracy of finite-difference and finite-element modeling of the scalar and elastic wave equations: Geophysics, **49**, 533–549, doi: 10.1190/1.1441689.

McMechan, G., 1983, Migration by extrapolation of time-dependent boundary values: Geophysical Prospecting, **31**, 413–420, doi: 10.1111/j.1365-2478.1983.tb01060.x.

Nardi, D., J. Sarout, A. Bóna, and D. Dewhurst, 2012, Estimation of the anisotropy parameters of transversely isotropic shales with a tilted symmetry axis: Geophysical Journal International, **190**, 1197–1203, doi: 10.1111/j.1365-246X.2012.05545.x.

Pecorari, C., 2003, Nonlinear interaction of plane ultrasonic waves with an interface between rough surfaces in contact: Journal of the Acoustical Society of America, **113**, 3065–3072, doi: 10.1121/1.1570437.

Pouet, B., and P. Rasolofosaon, 1990, Seismic physical modeling using laser ultrasonics: 60th Annual International Meeting, SEG, Expanded Abstracts, 841–844.

Prasad, M., 2003, Velocity-permeability relations within hydraulic units: Geophysics, **68**, 108–117, doi: 10.1190/1.1543198.

Prasad, M., and M. H. Manghnani, 1997, Effects of pore and differential pressure on compressional wave velocity and quality factor in Berea and Michigan sandstones: Geophysics, **62**, 1163–1176, doi: 10.1190/1.1444217.

Pyrak-Nolte, L., L. Myer, and N. Cook, 1990, Transmission of seismic waves across a single natural fracture: Journal of Geophysical Research, **95**, 8617–8638, doi: 10.1029/JB095iB06p08617.

Sarout, J., L. Esteban, C. D. Piane, B. Maney, and D. Dewhurst, 2014, Elastic anisotropy of Opalinus Clay under variable saturation and triaxial stress: Geophysical Journal International, **198**, 1662–1682, doi: 10.1093/gji/ggu231.

Scales, J. A., and A. E. Malcolm, 2003, Laser characterization of ultrasonic wave propagation in random media: Physical Review E, **67**, 046618, doi: 10.1103/PhysRevE.67.046618.
Scruby, C., and L. Drain, 1990, Laser ultrasonics techniques and applications 1st ed.: Taylor & Francis.
Shragge, J., 2014a, Reverse time migration from topography: Geophysics, **79**, no. 4, S141–S152, doi: 10.1190/geo2013-0405.1.
Shragge, J., 2014b, Solving the 3D acoustic wave equation on generalized structured meshes: A finite-difference time-domain approach: Geophysics, **79**, no. 6, T363–T378, doi: 10.1190/geo2014-0172.1.
Sondergeld, C. H., and C. S. Rai, 2011, Elastic anisotropy of shales: The Leading Edge, **30**, 324–331, doi: 10.1190/1.3567264.
Tarantola, A., 1984, Inversion of seismic reflection data in the acoustic approximation: Geophysics, **49**, 1259–1266., doi: 10.1190/1.1441754.
Todd, T., and G. Simmons, 1972, Effect of pore pressure on the velocity of compressional waves in low-porosity rocks: Journal of Geophysical Research, **77**, 3731–3743, doi: 10.1029/JB077i020p03731.
Tompkins, M., and N. Christensen, 2001, Ultrasonic P-and S-wave attenuation in oceanic basalt: Geophysical Journal International, **145**, 172–186, doi: 10.1046/j.0956-540x.2001.01354.x.
Vanorio, T., M. Prasad, D. Patella, and A. Nur, 2002, Ultrasonic velocity measurements in volcanic rocks: Correlation with microtexture: Geophysical Journal International, **149**, 22–36, doi: 10.1046/j.0956-540x.2001.01580.x.
Vialle, S., and T. Vanorio, 2011, Laboratory measurements of elastic properties of carbonate rocks during injection of reactive CO_2-saturated water: Geophysical Research Letters, **38**, L01302, 10.1029/2010GL045606.
Wang, Z., 2002, Seismic anisotropy in sedimentary rocks. Part 2: Laboratory data: Geophysics, **67**, 1423–1440, doi: 10.1190/1.1512743.
Whitmore, N., and S. Crawley, 2012, Applications of RTM inverse scattering imaging conditions: 82nd Annual International Meeting, SEG, Expanded Abstracts, 779–784.
Whitmore, N. D., 1983, Iterative depth imaging by backward time propagation: 53rd Annual International Meeting, SEG, Expanded Abstracts, 382–384.
Winkler, K. W., 1985, Dispersion analysis of velocity and attenuation in Berea sandstone: Journal of Geophysical Research: Solid Earth, **90**, 6793–6800, doi: 10.1029/JB090iB08p06793.